






Preservation of Discrete Morse-Smale Complexes in Error-Bounded Lossy Compression

Yuxiao Li , Mingze Xia , Xin Liang , Bei Wang , Hanqi Guo 

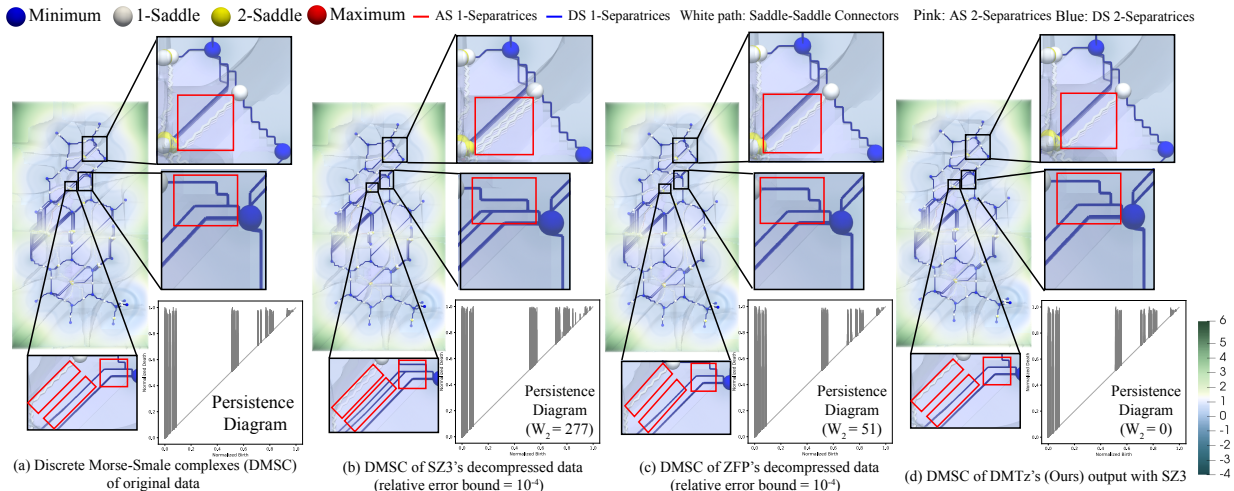


Fig. 1: Morse-Smale complexes of the Adenine Thymine (AT) dataset extracted from (a) the original data, (b) SZ3's decompressed data, (c) ZFP's decompressed data, and (d) DMTz's output with SZ3. All compression results use a relative error bound of 10^{-4} . We also visualize the persistence diagrams in Figures (a)–(d), where both birth and death values are normalized. W_2 denotes the L^2 –Wasserstein distance between each output's persistence diagram and that of the original data, quantifying the topological distortion.

Abstract— We propose a novel method to preserve key topological structures—extrema, saddles, separatrices, and persistence diagrams—associated with Morse-Smale complexes in error-bounded lossy compressed scalar fields. Existing error-bounded lossy compressors rarely consider preserving topological structures such as discrete Morse-Smale complexes, leading to significant inaccuracies in data interpretation and potentially resulting in incorrect scientific conclusions. This paper mainly focuses on preserving the Morse-Smale complexes in 2D/3D discrete scalar fields by precisely preserving critical points (cells) and the separatrices that connect them. Our approach generates a series of (discrete) edits during compression time, which are applied to the decompressed data to accurately reconstruct the complexes while maintaining the error within prescribed bounds. We design a workflow that iteratively fixes critical cells and separatrices in alternating steps until convergence within finite iterations. Our approach addresses diverse application needs by offering users multiter options to balance compression efficiency and feature preservation. To enable effective integration with lossy compressors, we use GPU parallelism to enhance the performance of each workflow component. We conduct experiments on various datasets to demonstrate the effectiveness of our method in accurately preserving Morse-Smale complexes.

Index Terms—Lossy compression, feature-preserving compression, Morse-Smale complexes.

1 INTRODUCTION

The rapid advancement of scientific computing and engineering simulations generates a large volume of scientific data, posing significant challenges to scientists in data storage and visualization. Error-bounded lossy compression techniques [31, 34–36, 50, 60, 61] have been widely adopted to address data challenges by achieving significant compression ratios through controlled errors in decompressed data.

However, existing error-bounded lossy compressors do not explicitly consider the preservation of topological structures. Compression-

induced errors can distort the topology of the data [17, 29, 32, 56, 59], such as Morse-Smale complexes (MSC) [11, 12] (and their induced segmentations [29, 42]), and merge/contour trees [6, 17, 59], leading to inconsistencies between the topology of the original and decompressed data. Such topological inconsistencies can result in the misinterpretation of scientific results and unreliable feature extraction in fields such as chemistry [3, 21], material science [19, 44], climate [9], medical imaging [58], and cosmology [47]. For example, in molecular electron density analysis [3], as exemplified in Figure 1 (a), maxima correspond to locations of atomic nuclei; 2-saddle points represent bonds between atoms; 1-saddle points correspond to the centers of ring structures; and minima indicate cavity regions enclosed within molecular structures. The separatrices connecting these critical points represent atomic interaction paths, commonly interpreted as bond paths in chemical analyses. Thus, distortions introduced by lossy compression may significantly alter these critical features, potentially leading to severe errors in the interpretation of molecular structures. For instance, the disappearance of 2-saddle points may incorrectly suggest the absence of critical chemical bonds, while the emergence of non-existent critical points may mislead chemists into identifying false molecular cages or nuclei, leading to incorrect conclusions and analyses.

- Yuxiao Li and Hanqi Guo are with The Ohio State University. E-mail: {li.14025\guo.2154}@osu.edu.
- Mingze Xia and Xin Liang are with the University of Kentucky. E-mail: {mingze.xia\liang}@uky.edu.
- Bei Wang is with the University of Utah. E-mail: beiwang@sci.utah.edu.

Manuscript received xx xxx. 201x; accepted xx xxx. 201x. Date of Publication xx xxx. 201x; date of current version xx xxx. 201x. For information on obtaining reprints of this article, please send e-mail to: reprints@ieee.org. Digital Object Identifier: xx.xxx/TVCG.201x.xxxxxx

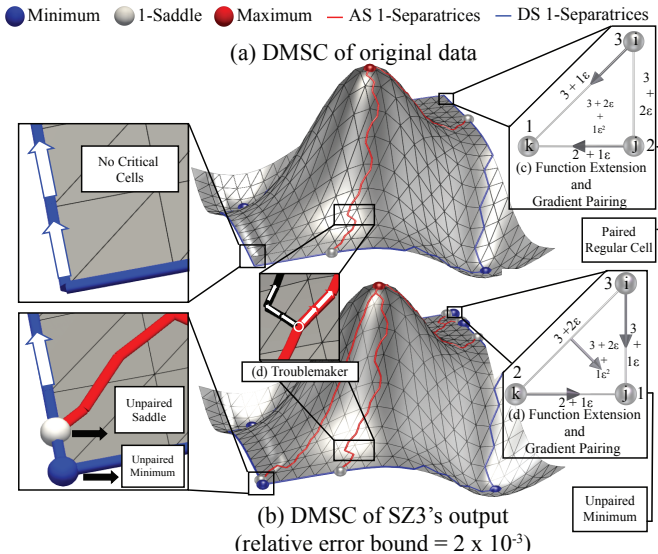


Fig. 2: Impacts of lossy compression (SZ3) on MSC under a relative error bound of 2×10^{-3} with synthetic data. DMSC of (a) the original data and (b) SZ3's output. (c) and (d) Function Extension and Gradient Pairing.

While it seems possible to mitigate topological inconsistencies by storing the original MSC alongside the compressed data, it still fails to align with the decompressed data, as demonstrated in our experiments. In Figure 1 (b) and (c), separatrices extracted from the decompressed data are misaligned with the original structures, and storing the original MSC no longer reflects the altered scalar field, resulting in inconsistencies in visualization and analysis. Therefore, rather than storing the original MSC, it is essential to preserve the topology during the compression process to ensure reliable scientific interpretation, as we demonstrate later in our experiments.

To the best of our knowledge, this work is the first to fully preserve the MSC within decompressed data under error-bounded lossy compression. The closest related method is MSz [29], which preserves topological segmentations induced by MSC, but MSz does not fully preserve the MSC. One key limitation is that MSz does not guarantee saddle points, which play a crucial role in MSC. In climate research, for instance, scientists rely on saddle points to identify potential turning points in storm paths [9]. Distorted saddle points can mislead weather forecasts, potentially leading to inadequate responses to extreme weather events.

In this paper, we introduce **DMTz**, an iterative workflow for preserving the discrete Morse-Smale complexes (DMSC) in 2D/3D scalar fields by correcting the outputs of error-bounded lossy compressors. Our method ensures the preservation of all critical points (including saddles) and the separatrices connecting these critical points. We chose DMSC as our preservation target due to its robust implementation and widespread use in scientific applications, including its adoption in production topological visualization tools such as the Topology Toolkit (TTK) [43]. Our method keeps the decompressed data within the user-defined error bound and could be integrated with any error-bounded lossy compressor by directly operating on the compression outputs. For a clearer comparison of the topological preservation capabilities of DMTz against other existing technologies, see our discussion later.

DMTz uses an iterative workflow with two subloops: (1) the critical cells loops (C-loops), which preserve the type and location of the critical cells, and (2) the separatrices loops (S-loops), which detect and fix the inaccuracies in the separatrices. Through a finite number of iterations, the workflow identifies a subset of data that requires edits, ensuring that the MSC in the decompressed data remains consistent with those in the original dataset while guaranteeing the global error bound. Moreover, we enhanced the edit compression method by converting

most edits into a quantized form, thereby reducing the average storage overhead required for storing the edits. We also used GPU parallelism to accelerate each workflow component.

We further propose a multitier topology preservation paradigm to support diverse scientific needs, enabling users to balance compression efficiency and topological preservation based on application goals. For example, medical imaging applications may focus on preserving extrema, such as intensity peaks corresponding to tumors or lesions [58], and atmospheric river analysis often relies on preserving the connectivity structure or topological skeleton [27], while combustion simulations require accurate preservation of saddle points and their connections to extrema [4, 5]. In summary, the contributions of this paper are:

- We developed an iterative workflow tailored for preserving Morse-Smale complexes within error-bounded lossy decompressed data in 2D/3D scalar fields, theoretically applicable to any existing error-bounded lossy compressors.
- We defined a multitier feature preservation goal, considering the topological feature requirements across different applications.
- We generalized the method for compressing the edits in MSz [29] by converting most edits into a quantized form, resulting in an overall reduced storage overhead.
- We conducted a comprehensive evaluation using various datasets from different applications and three off-the-shelf base compressors: SZ3 [34], ZFP [35], and TTHRESH [1].

2 RELATED WORK

We review related work on lossy compression, topology-preserving compression, and topological simplification and smoothing.

2.1 Lossy Compression

Lossy compression methods can be categorized as error-bounded and non-error-bounded based on whether the pointwise error is limited by user-defined bounds. Non-error-bounded methods can often achieve higher compression ratios while not constraining pointwise error within user-defined bounds. For example, neural network-based approaches, such as autoencoders [40] and implicit neural representations [18, 41], optimize for global reconstruction quality or perceptual similarity without providing explicit error guarantees. This work focuses on error-bounded lossy compression, which provides more precise control over data distortion, as discussed later.

Error-bounded lossy compression achieves efficient data compression while ensuring that the introduced error remains within the user-defined error bound, providing high data quality. Error-bounded compression methods can be divided into prediction-based and transformation-based approaches. Prediction-based methods, like the SZ series [23, 24, 31, 34, 39, 50, 60], estimate data points using predictors such as Lorenzo and then quantize the residuals for compression. Recent works further explore neural networks to improve prediction accuracy, including AE-SZ [38] and SRNN-SZ [37]. FPZIP [36] and ISABELA [26] follow similar prediction-based approaches with bit-plane truncation and B-spline transformations, respectively. Transformation-based compressors, like ZFP [35], TTHRESH [1], SPERR [28], and MGARD [16], apply techniques like wavelet transforms or tensor decompositions to compress data more efficiently. For a more comprehensive survey of error-bounded lossy compression methods for scientific datasets, we refer readers to Di et al. [8].

2.2 Topology-Preserving Compression of Scalar-Field Data

To the best of our knowledge, our work is the first attempt to fully preserve MSC within error-bounded lossy compression. Note that the pointwise error bound is still important in the context of topology preserving compression beyond topological data analysis (TDA), as many downstream applications and checkpoint-restart simulations rely on local data accuracy, and uncontrolled errors can significantly affect the integrity of scientific results such as statistical analysis. To achieve topological preservation in error-bounded lossy compression, one needs to modify the compression workflow. We classify these modifications into the following three categories.

The first strategy is to **modify the input scalar field** before compression to guide the preservation of topological features. For example, Soler et al. [49] proposed a topology-controlled compression method that preserves the persistence diagram by adaptively quantizing data based on a persistence simplification threshold. Their approach relies on the input of the persistence threshold for pointwise error control. In contrast, our method targets a different topological descriptor, MSC, and is parameter-independent.

The second strategy is to **modify specific compression algorithms** directly, but the modification is specific to a compressor, limiting the broader applicability. For example, Yan et al. [59] proposed TopoSZ, incorporating topological constraints derived from segmentations guided by contour trees by modifying the SZ 1.4 [31] compression algorithm.

The third strategy is to **correct the decompressed data** to preserve topological features, but existing methods do not support the preservation of the full MSC. For example, Gorski et al. [17] proposed a framework that clamping the values of decompressed data to preserve contour trees. Li et al. [29] proposed MSz, an edit-based method for preserving MS segmentations in 2D/3D piecewise linear scalar fields by focusing on extrema and the integral lines connecting them by deriving a series of edits applied to the decompressed data during compression.

As related, the community has also explored topology preservation in vector fields. For example, Liang et al. [30,33] and Xia et al. [56,57] proposed compressor-specific strategies that preserve critical points and topological skeletons by incorporating topological constraints into the compression pipeline. Theisel et al. [51] proposed a method that first modifies the vector field to simplify its topology before applying compression. Tricoche et al. [53] collapse edges in a 2D mesh to guarantee topology preservation.

2.3 Topological Simplification and Smoothing

Although closely related, topological simplification and smoothing serve fundamentally different goals than topology-preserving compression. As general techniques, they are widely used in data analysis and visualization to reduce topological complexity or remove noise by modifying the data. While it may be possible to incorporate simplification or smoothing into compression pipelines, these approaches are not designed to retain detailed topological structures under strict point-wise error bounds, as demonstrated later.

Topological simplification and smoothing techniques can be broadly categorized into approaches for both scalar fields and vector fields. For scalar fields, simplification techniques remove low-persistence features by canceling pairs of critical points [20,52]. Optimization-based methods, such as solver-based smoothing [25], adjust scalar values to approximate a target persistence diagram. Other techniques reconstruct the scalar field using monotonicity constraints [22] or enforce smoothness via C^1 -continuity while preserving selected features [54].

For vector fields, simplification methods focus on reducing topological noise while retaining important flow features. For example, Weinkauff et al. [55] extract higher-order critical points in 3D fields, and Wang et al. [48] introduce hierarchical simplification based on robustness for steady and unsteady 2D fields.

3 BACKGROUND

We review the background of Morse-Smale complexes and topology preservation with edits in error-bounded lossy compression.

3.1 Morse-Smale Complexes

In TDA, one of the most effective tools for understanding the structure of scalar fields is MSC. By identifying critical points (maxima, minima, and saddles) and connecting them via integral lines, MSC decomposes the domain into regions of uniform gradient behavior, revealing essential topological features in the data. Two distinct types of theories exist for computing MSC: the discrete Morse theory [14] and the piecewise linear (PL) Morse theory [2,12]. Each approach offers distinct advantages depending on the structure of the input data and the computational requirements; for a detailed comparison between the discrete Morse theory and PL Morse theory, refer to [7].

3.2 Discrete Morse-Smale Complexes

We build upon the general concept of MSC using the discrete Morse theory introduced by Forman [15], which defines a *discrete gradient field* on a cell complex. A (simplicial) *cell complex* is an abstract representation of a mesh composed of vertices (*0-cells*), edges (*1-cells*), triangles (*2-cells*), and higher-dimensional cells. A *facet* refers to the $(k-1)$ -dimensional face of a k -dimensional cell, while a *cofacet* is the $(k+1)$ -dimensional cell that contains the k -dimensional cell as its face. A *discrete gradient field* consists of pairings between incident cells whose dimensions differ by one, with the constraint that each cell appears in at most one pair. For example, in Figure 2(c), vertex i is paired with its cofacet edge ij (the rationale for such pairings will be explained later). Cells that are not involved in any pairing are identified as *critical cells*, corresponding to topological features such as minima, saddles, and maxima. For instance, vertex j in Figure 2(d) is a minimum because it is unpaired. A *gradient path* is a sequence of cells paired through the gradient pairing process (e.g., 0-cell, 1-cell, 0-cell), and gradient paths that connect critical cells correspond to separatrices in Morse theory, as the red and blue paths shown in Figure 2 (a) and (b). Separatrices that connect 1-saddles to 2-saddles are specifically referred to as saddle-saddle connectors.

A critical step in computing the DMSC from a scalar field is extending scalar values from vertices to higher-dimensional cells to enable valid gradient pairings, as scalar fields in practice are typically defined only on vertices. There exist several function extension methods for constructing discrete Morse functions, we adopt the method of Shivashankar et al. [46] because it is well-suited for parallel implementation and avoids explicit function computation by relying solely on local order comparisons among vertices (a comparison between our approach using the method proposed by Shivashankar et al. [46] and that of Robins et al. [45] is provided in the appendix). Specifically, the discrete Morse function F is recursively extended to a d -dimensional cell α as:

$$F(\alpha) = F(G_0(\alpha)) + \varepsilon^d F(G_1(\alpha)), \quad (1)$$

where ε is a (symbolic) perturbation to enforce strict ordering, $G_0(\alpha)$ is the highest-valued face of α , and $G_1(\alpha)$ is the highest among the remaining non-adjacent faces. We define P_α as the set of $(d+1)$ -dimensional cofacets β such that α is the highest-valued facet of β under the extended function. For example, for edge ij in Figure 2 (c), $G_0(ij)$ is vertex i , $G_1(ij)$ is vertex j and P_{ij} is triangle ijk .

Figure 2(c) illustrates the function extension and gradient pairing rules used to construct the discrete gradient vector field. The scalar field f is defined only on vertices: $f_i = 3$, $f_j = 2$, and $f_k = 1$. These values are recursively extended to higher-dimensional cells using Equation (1). For example, the extended function value of edge ij is $F_{ij} = f_i + \varepsilon f_j = 3 + 2\varepsilon$, and for edge ik , $F_{ik} = 3 + \varepsilon$.

Based on the extended function F of the original scalar field f , the discrete gradient field is constructed by pairing each d -dimensional cell α with the $(d+1)$ -dimensional cofacet in P_α that has the smallest function value. For example, in Figure 2(c), vertex i is the highest-valued facet of both edges ij and ik . Because $F_{ik} = 3 + \varepsilon < F_{ij} = f_j = 3 + 2\varepsilon$, edge ik is the lowest-valued cofacet in P_i , and vertex i is therefore paired with edge ik .

The function extension and gradient pairing method implies that errors introduced by lossy compression can propagate from vertex scalar values to the extended function values of higher-dimensional cells, leading to incorrect gradient pairings and distorting the topology. As illustrated in Figure 2(c), in the original data f , the pairing of vertex j is paired with edge jk because $f_j = 2 > f_k = 1$. However, in the decompressed data \hat{f} (Figure 2(d)), compression-induced error alter the vertex scalar values such that $\hat{f}_j = 1 < \hat{f}_k = 2 < \hat{f}_i = 3$. As a result, vertex j , which was originally a regular cell paired with edge jk , becomes unpaired and is incorrectly identified as a minimum.

3.3 Comparison of Piecewise Linear MSC (PLMSC) and DMSC in Topology Preservation

An alternative approach to defining MSC in discrete data is the PLMSC, which constructs the MSC based on comparing vertex scalar values. In

this work, we choose to focus on DMSC due to its robust implementation and widespread use in scientific applications [43]. For a detailed comparison between PLMSC and DMSC, we refer the reader to [7]. In terms of topology preservation, DMSC poses a greater challenge due to its multi-dimensional cell dependencies. In DMSC, a vertex’s scalar value influences not only adjacent vertices but also higher-dimensional cells such as edges, triangles, and tetrahedra. Consequently, any modification to a vertex value may influence the gradient field across different dimensions. In contrast, PLMSC is constructed through local comparisons between vertices, where changes to a vertex value only affect its immediate neighborhood without influencing other dimensions.

3.4 Edit-based Strategy for Topology Preserving Compression

We refer to the edit-based strategy as an approach that generates a series of targeted edits to the decompressed data to recover the desired topological structures while maintaining the prescribed error bounds ξ . This strategy was first proposed in MSz [29] for preserving topological features in lossy compression. In this work, we generalize their edit-based strategy to support the multitier preservation of DMSC.

The edit-based strategy is effective for preserving feature descriptors relying on the ordering of data, such as MS segmentations and MSC, because it modifies the values of a subset of data points to preserve the local data ordering necessary for preserving the target features. Because the edits are directly applied to the decompressed data, this method can be applied to any existing error-bounded lossy compressor without being tied to the specific compression algorithm.

The edit-based strategy involves identifying distorted features, such as critical points, during each iteration and modifying the scalar value of specific data points to correct these distortions. Assume that vertex i a regular cell paired with edge ij in the original data f and vertex j is one of its neighbors, such that $f_i > f_j$. In the decompressed data \hat{f} as shown in Figure 3, vertex i become a minimum as $\hat{f}_i < \hat{f}_j$, in this case we can fix the topological inconsistency by decreasing the value of the vertex j such that $\hat{f}_i > \hat{f}_j$, making vertex i paired with edge ij . However, the modification may introduce new distortions, leading to further iterations. The process continues until all targeted features are accurately preserved.

The key to the convergence of the iterative process is that the edits applied to each data point are either negative or zero. Specifically, for a data point i at iteration k , the edited scalar value $g_i^{(k)}$ satisfies: $\hat{f}_i = g_i^{(0)} \geq \dots \geq g_i^{(k)} \geq g_i^{(k+1)} \geq \dots \geq f_i - \xi$, where \hat{f}_i is the initial decompressed value, f_i is the original value, and ξ is the absolute error bound. Since the original data has an inherent order, and the edits on data point i are always negative or zero, one can always find a finite iteration k where the scalar value of i and its neighbors align with the original data’s order. In the worst-case scenario, all data values may decrease to the lower bound $f_i - \xi$, under which the data ordering will remain consistent with that of the original data, thus guaranteeing convergence.

While edit-based methods enable topological feature preservation, storing edits comes with a cost. To address the storage overhead introduced by edits, we propose a quantization strategy (referred to as *quantized edits*) that stores most edits in a quantized form, with only a small subset needing to be stored losslessly. The quantized edits significantly reduce the overall storage cost without affecting feature accuracy, in contrast to MSz, which stores all edits losslessly (referred to as *floating-point edits*). Later, we demonstrate the effectiveness of

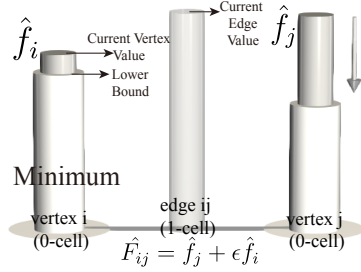


Fig. 3: Illustration of the edit-based strategy: vertex i , originally a regular cell paired with edge ij , becomes an unpaired minimum after decompression. The height of each bar above a cell represents its current scalar value.

our quantized edits in our experiments.

4 PROBLEM STATEMENT AND METHODOLOGY

In this section, we formally define the problem of preserving the DMSC in error-bounded lossy compression and present our methodology, which iteratively corrects compression-induced distortions while ensuring the error bound is maintained.

Notations used throughout our paper are as follows: ξ represents the user-defined error bound, and i denotes the i th vertex, edge ij refers to the edge consisting of vertices i and j , triangle ijk denotes the triangle formed by vertices i , j and k , and tetrahedron $ijkl$ represents the tetrahedron consisting of vertices i , j , k and l . The scalar values at vertex i in the original and decompressed data are represented by f_i and \hat{f}_i , respectively, while g_i refers to the edited scalar value at vertex i . For a given cell α , P_α denotes the set of $(d+1)$ -dimensional cofacets β for which α is the maximum-valued facet of β .

4.1 Problem Statement

We formulate the multitier preservation of MSC in 2D and 3D scalar fields under error-bounded lossy compression. The inputs of our algorithm include the original scalar field f and the decompressed field \hat{f} , both defined on the same cell complex with the same number of vertices. We assume all scalar fields are Morse, i.e., for any two vertices i and j , $f_i \neq f_j$; otherwise, simulation of simplicity (SoS) [13] is applied to handle degenerate cases.

The output of our algorithm is a set of edits $\{\delta_i\}$, where each edit adjusts the scalar value of a vertex i to obtain the final edited value $g_i = \hat{f}_i + \delta_i$. Our method ensures the following preservation constraints: **Preservation of the global error bound.** We guarantee that the final edited scalar field g strictly satisfies the user-prescribed absolute error bound ξ , that is, $|f_i - g_i| \leq \xi$.

Multitier Preservation targets. Tier 1 (Extrema Preservation): Ensures that any cell identified as an extrema in the original data retains both its critical type and location in the decompressed data, while cells that are not extrema in the original data remain non-extrema after decompression. Tier 2 (Critical Cells Preservation): Extends Tier 1 by additionally preserving saddle points. Tier 3 (Connectivity Preservation): Ensures that each saddle in the decompressed data connects to the same set of extrema as in the original data. Tier 4 (Separatrix Preservation): Ensures that the separatrices that connect critical cells in the decompressed data follow the same paths as in the original data. Tier 5 (Persistence Diagram Preservation): Ensures that the persistence diagram of the decompressed data matches that of the original data.

4.2 Methodology

Our methodology corrects distortions in the DMSC by editing vertex values to fix incorrect gradient pairings introduced by compression-induced errors. We design an iterative workflow to compute vertex-wise edits during compression, as illustrated in Figure 4. The workflow alternates between two main loops: **critical cells loops (C-loops)**: correct false critical cells, preserving extrema (T1) and saddles (T2–T5). **separatrices loops (S-loops)**: correct false separatrices, preserving saddle-extrema connectivity (T3) and geometric separatrices (T4, T5).

The key insight is that modifying vertex values directly alters the extended function values of higher-dimensional cells (edges, triangles, tetrahedra) through Equation (1). Since gradient pairings depend entirely on these relative extended function values, adjusting vertex values enables us to recover correct pairings and preserve the DMSC structure. For a better understanding of our methodology, we summarize the pairing rules derived from the approach proposed by Shivashankar et al. [46], after using Equation(1) to extend function value to higher-dimensional cells: **vertex i** is paired if there exists at least one adjacent vertex j such that $f_i > f_j$, and it pairs with the edge ij where f_j is minimal among all such j ; **edge ij** is paired if either (1) it has been paired by a vertex, and (2) there exists a triangle ijk such that $\min(f_i, f_j) > f_k$, in this case, the edge pairs with the triangle ijk where f_k is minimal among all such k ; **triangle ijk** is paired if either (1) it is paired with an edge, and (2) there exists a **tetrahedron $ijkl$** such that $\min(f_i, f_j, f_k) > f_l$.

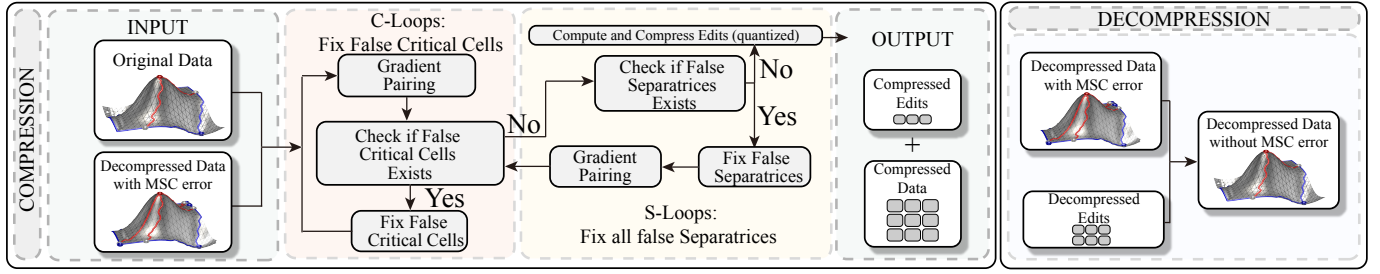


Fig. 4: An illustration of the workflow of our algorithm for preserving the full MSC. Our algorithm gets a series of edits during the compression time with two distinct loops: (1) C-loops, which iteratively fix all false critical cells, and (2) S-loops, which iteratively fix all false separatrices. The C-loops and S-loops alternate until no false critical cells or separatrices exist. The quantized edits are losslessly compressed and included with the compressed data in the compression output. The edits are applied to the decompressed data to correct MSC in the decompression stage.

in this case, the triangle pairs with the tetrahedron $ijkl$ where f_i is minimal among all such l .

Specifically, in each loop, we identify a vertex i responsible for incorrect gradient pairing. This vertex is either part of a false critical cell or a *troublemaker* (the first cell along a separatrix where the gradient pairing result is incorrect, as shown in Figure 2(d)). Once identified, we gradually decrease its scalar value to recover the correct gradient pairing result. Let q_{\max} be a user-defined hyperparameter that controls the edit step size, where each edit decreases the scalar value of a vertex i by $\xi/2^{q_{\max}}$, q denote the number of edits applied to i , and $g_i^{(k)}$ is the edited value at iteration k . The scalar value of vertex i is updated iteratively as follows:

$$g_i^{(k+1)} = g_i^{(k)} - \xi/2^{q_{\max}}, \text{ if } q < q_{\max} \text{ and } g_i^{(k)} - \xi/2^{q_{\max}} \geq f_v - \xi. \quad (2)$$

The edit continues until either q reaches q_{\max} or further edit exceeds the lower bound $f_i - \xi$. In either case, the final edit δ_i is stored losslessly. For example, assume that vertex i is first edited from \hat{f}_i to $g_i^{(1)} = \hat{f}_i - \xi/2^{q_{\max}}$, then to $g_i^{(2)} = \hat{f}_i - 2 \cdot \xi/2^{q_{\max}}$, and so on. The edit continues until either $q = q_{\max}$, or $g_i^{(k+1)} \leq f_i - \xi$. At that point, we set $g_i = f_i - \xi$, and losslessly store the edit $\delta_i = f_i - \xi - \hat{f}_i$.

4.3 Critical Cells Loops (C-Loops)

The C-loops focus on fixing all false critical cells, including false positive/negative minima, saddles, and maxima. *False positive* cases are defined as cells paired with their facet/cofacet in the original data but not paired with any in the decompressed data. Conversely, *false negative* cases are cells that were unpaired in the original data but paired with one of their facets/cofacets in the decompressed data. We will discuss the method for selecting the vertex i that needs editing in different cases below. For false positive/negative minima, we describe the fix process in detail, while for the remaining cases, we focus on the overall editing strategy and omit intermediate steps for brevity.

False Positive Minimum (FPmin). Based on the gradient pairing rules summarized above, an FPmin is a vertex i that is paired with an adjacent edge ij in the original data because there exists at least one adjacent vertex j such that $f_i > f_j$. However, after decompression, $\hat{f}_i < \hat{f}_j$ holds for all adjacent vertices j , causing vertex i to become unpaired and incorrectly identified as a minimum.

We use Figure 5 to explain this case further. Assume that vertex i is a regular cell paired with edge ij in the original data, meaning $f_i > f_j$. However, after compression, as shown in Figure 5(a), vertex i becomes an FPmin because $\hat{f}_i < \hat{f}_j$. As a result, vertex i remains unpaired and is incorrectly identified as a minimum. To correct this, our method identifies vertex j for editing. By decreasing \hat{f}_j as shown in Figure 5(b), the condition $g_i > g_j$ is restored. This enables vertex i to pair with edge ij , eliminating the FPmin.

False Negative Minimum (FNmin). Assume that vertex i is an unpaired minimum in the original data, meaning that $f_i < f_j$ for all adjacent vertices j . After decompression, as illustrated in Figure 5(c),

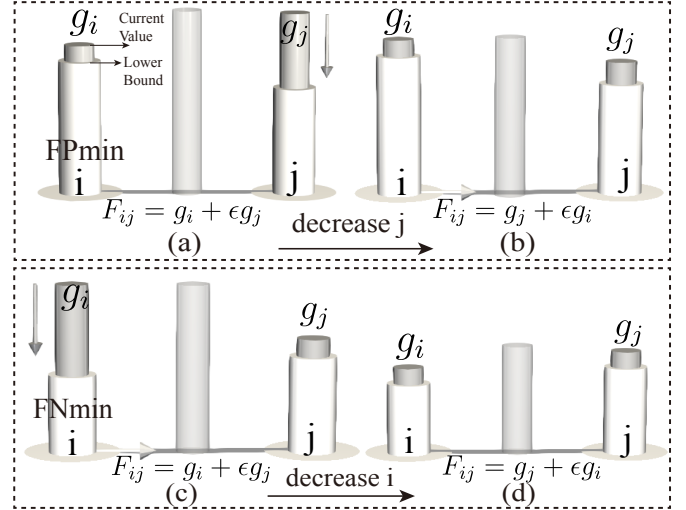


Fig. 5: Fixing an FPmin/FNmin vertex i . (a) and (b) illustrate the process for fixing FPmin, while (c) and (d) demonstrate the process for FNmin. The height of the white cylinder above each vertex represents its lower bound ($f - \xi$), the height of the gray cylinder represents its current value, and the height of the translucent gray cylinder above the edge represents its current extended function value. The arrow from vertices to edges indicates the gradient pairing results.

$\hat{f}_i > \hat{f}_j$, making vertex i incorrectly paired with edge ij , turning it into a FNmin. To fix this, we decrease g_i until $g_i < g_j$. Once corrected, vertex i no longer dominates any adjacent edge and returns to being an unpaired minimum, as shown in Figure 5(d).

False Positive 1-Saddle (FP1saddle). According to the gradient pairing process, an FP1saddle edge ij in the original data should be paired in one of the two conditions: **1.** paired with a vertex v_i , requiring $f_i > f_j$; **2.** paired with a triangle ijl , requiring $f_i > f_l$ and $f_j > f_l$. However, in the decompressed data, the vertices forming the FP1saddle edge ij do not satisfy either of the above conditions; therefore, we can modify the gradient pairing result by editing one of the vertices associated with the vertex or triangle paired with edge ij in the original data, as shown in Figure 6 (a)-(d).

False Negative 1-Saddle (FN1saddle) could be fixed by making it unpaired in the decompressed data. If an FN1saddle edge ij is paired with vertex i in the decompressed data (as shown in Figure 6(e) and (f)), we decrease vertex i so that $g_i < g_j$, preventing edge ij from pairing with vertex i . Similarly, if it is paired with triangle ijl (as shown in Figure 6(g) and (h)), we decrease either vertex i or vertex j , ensuring that edge ij cannot pair with triangle ijl .

False Positive 2-Saddle (FP2saddle). An FP2saddle triangle ijk in the original data should be paired with an edge/tetrahedron in one of the two conditions: **1.** paired with edge ij , requiring $f_i > f_k$ and $f_j > f_k$; **2.**

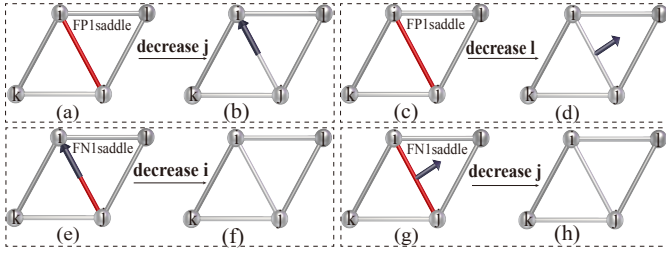


Fig. 6: Fixing an FP1saddle that should be paired with a vertex: (a) and (b), or a triangle: (c) and (d), and an FN1saddle that incorrectly paired with a vertex: (e) and (f), or a triangle: (g) and (h).

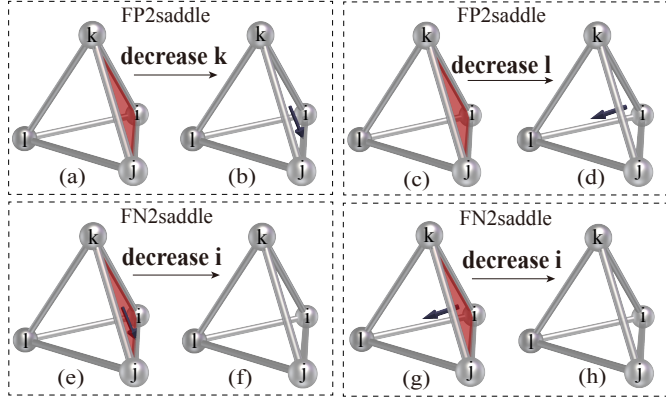


Fig. 7: Fixing an FP2saddle that should be paired with an edge: (a) and (b), or a tetrahedron: (c) and (d), and an FN2saddle that incorrectly paired with an edge: (e) and (f), or a tetrahedron: (g) and (h).

paired with tetrahedron $ijkl$, requiring $f_i > f_l$ and $f_j > f_l$ and $f_k > f_l$. Similar to the FP1saddle case, we can edit one of the vertices associated with the edge or tetrahedron paired with triangle ijk in the original data, as shown in Figure 7.

False Negative 2-Saddle (FN2saddle). Similar to the FN1saddle cases, if an FN2saddle is incorrectly paired with an edge ij then we edit vertex i or j (as shown in Figure 7(e) and (f)); if it is paired with a tetrahedron $ijkl$, then we edit vertex i or j or l (as shown in Figure 7(g) and (h)).

False Positive maximum (FPmax). In 2D, maxima is represented by a triangle, while in 3D, it is represented by a tetrahedron. Therefore, we discuss these cases separately. In a 2D case, as shown in Figure 8(a) and (b), triangle ijk is an FPmax which is paired with edge ik in the original data (as shown in Figure 8(b)), meaning the scalar values of vertex i , vertex k , and vertex j must satisfy that $f_i > f_j$ and $f_k > f_j$. We then decrease the value of vertex j until this condition is also satisfied in the decompressed data. In a 3D case, the FPmax is a tetrahedron $ijkl$, as shown in Figure 8(e) and (f). Assuming that tetrahedron $ijkl$ is paired with a triangle ijk in the original data. Similarly, we decrease vertex l .

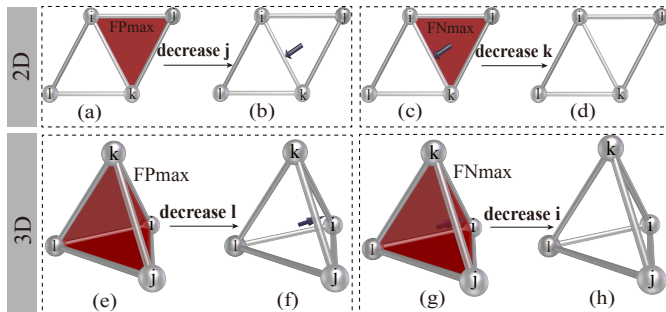


Fig. 8: Fixing an FPmax in 2D: (a) and (b), and in 3D: (e) and (f); and an FNmax in 2D: (c) and (d), and in 3D: (g) and (h).

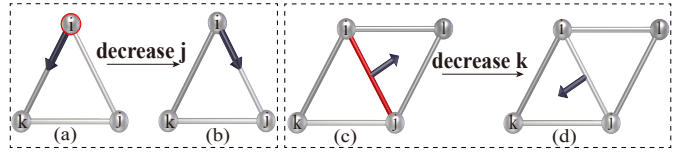


Fig. 9: Illustration of fixing troublemakers in 2D: (a) and (b) represent cases where the troublemaker is a vertex, while (c) and (d) represent cases where the troublemaker is an edge.

False Negative maximum (FNmax) could also be divided into two cases: In a 2D case, the FNmax is a triangle ijk , as shown in Figure 8(c). Assuming that triangle ijk is paired with an edge ik in the decompressed data, this implies that $\hat{f}_i > \hat{f}_j$ and $\hat{f}_k > \hat{f}_j$. We decrease vertex i or k to break this condition, leaving triangle ijk unpaired with any edge. In a 3D case, the FNmax is a tetrahedron $ijkl$ as shown in Figure 8(g). Assuming that tetrahedron $ijkl$ is paired with a triangle ijk in the decompressed data, similar to the 2D case, we decrease vertex i , j , or k to leave tetrahedron $ijkl$ unpaired.

4.4 Separatrices Loops (S-Loops)

After all false critical cells are fixed, we proceed to fix the incorrect gradient pairings encountered when tracing separatrices from each saddle. Each iteration of our method consists of three steps: (1) in the k th iteration, extract ascending/descending paths and saddle-saddle connectors from the current edited data $g^{(k)}$ based on gradient pairings; (2) identify the corresponding *troublemaker*; (3) edit the scalar value of vertices forming the *troublemaker* to correct the pairing.

The troublemaker may be a 0-cell (paired with an incorrect 1-cell in descending separatrices), a 1-cell (paired with an incorrect 2-cell in saddle-saddle connectors), or a 2-cell (paired with an incorrect 3-cell in ascending separatrices). We now analyze each case based on the different dimensions of the troublemaker.

A **0-dimensional** troublemaker vertex i , as shown in Figure 9(a) and (b), is incorrectly paired with edge ik in the decompressed data, whereas vertex i should be paired with edge ij in the original data. According to the gradient pairing rule, vertex i should pair with the edge in P_i that has the smallest function value. To correct this, we decrease vertex j , ensuring that vertex i pairs correctly with edge ij .

A **1-dimensional** troublemaker edge ij should pair with triangle ijk in the original data but is incorrectly paired with triangle ijl in the decompressed data (as shown in Figure 9(c) and (d), meaning that the function value of triangle ijk is greater than that of triangle ijl in \hat{f} . Note that triangles ijl and ijk share vertices i and j , so their scalar ordering is determined by the relative values of vertices k and l . We decrease vertex k , making edge ij pair correctly with triangle ijk .

The process is similar for a **2-dimensional** troublemaker triangle ijk . Suppose tetrahedron $ijkl$ is the tetrahedron paired with triangle ijk in the original data, and in the decompressed data, triangle ijk is paired with tetrahedron $ijkq$. For a similar reason as in the 2D troublemaker case, we decrease vertex l .

4.5 Convergence Analysis

Our workflow alternates between C-loops and S-loops to iteratively fix false critical cells and separatrices. Note that edits made during the C-loops may introduce new distortions in separatrices, while edits in the S-loops may create new false critical cells, we must iteratively excute C-loops and S-loops to address these newly introduced false cases. To ensure that this alternating procedure eventually terminates with the fully preserved MSC, we analyze the convergence of our method by first proving that each individual loop terminates and then demonstrating the convergence of the overall workflow.

Convergence of C- and S-Loops The false critical cells in the C-loops are caused by incorrect gradient pairing results, which are determined by the scalar value order of the vertices constituting each cell. Modifying the scalar values of the vertices modifies the scalar values of the associated cells, thereby correcting the gradient pairing results. However, modifying the scalar value of any vertex affects all

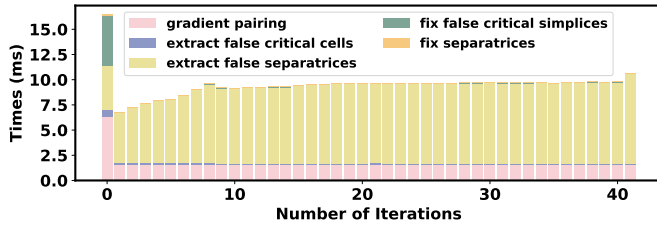


Fig. 10: Timings of different components per iteration on the Vortex dataset, using SZ3 as the base compressor.

cells containing the vertex, potentially introducing new false cases and requiring further iterations of the C-loop.

The iterative process of the C-loop is guaranteed to converge because gradient pairings depend solely on the scalar value order of vertices. Since all edits strictly decrease vertex values, and each vertex has a lower bound at $f_i - \xi$, no vertex can be edited infinitely many times. Even if a modification introduces new false critical cells, the total number of modifications is finite. In the worst case, all vertices reach their lower bound, at which point their relative order matches that of the original data. Once the scalar order is recovered, gradient pairing results are guaranteed to match those of the original data, eliminating all false critical cells. Therefore, the C-loop converges after a finite number of iterations. Similarly, modifications in the S-loops also strictly decrease vertex scalar values toward their lower bounds, ensuring the convergence of the S-loops for the same reason.

Convergence of Alternating C- and S-Loops. S-loops may introduce new false critical cells by modifying vertex values along separatrices. However, these new false critical cells are always corrected in subsequent C-loops. Since all edits strictly decrease vertex values and remain bounded, this alternating process cannot continue indefinitely. At worst, all vertices reach their lower bounds, ensuring that their relative scalar order is fully determined, restoring gradient pairings to match the original data. As a result, all false critical cells and separatrix distortions are eventually resolved, guaranteeing convergence within a finite number of iterations.

4.6 Multitier Preservation

We designed our method to support multiple tiers of topological feature preservation to accommodate different application needs while balancing efficiency and topology preservation. Our method allows early termination based on the selected tier. For example, T1 and T2 focus on preserving extrema or critical cells. In these cases, only C-loops are needed, and the process stops once all false extrema or critical cells are fixed. T3 also preserves the connectivity between saddles and extrema, so S-loops are used to detect and fix incorrectly connected critical cells. T4 further requires accurate gradient paths, which means more troublemakers must be identified and corrected compared to T3. For T5, we edit the scalar values of all vertices that constitute the critical cells in the original data to their lower bound $f - \xi$ before the iterative process begins. This is because preserving the persistence diagram requires maintaining the filtration order, meaning that the scalar value differences between each pair of connected critical cells must be exactly the same as the original data.

4.7 Quantized Representation of Edits

To reduce the storage overhead associated with storing edits, we propose a quantized representation that efficiently encodes edit values while maintaining feature preservation while MSz directly stores the edits δ_i as floating-point numbers using a key-value pair format. However, storing edits in floating-point representation incurs significant storage costs, particularly for large datasets or frequent edits.

In contrast, our method applies a fixed edit step of $\xi/2^{q_{\max}}$ at each iteration, as defined in Equation (2). The quantized form allows us to store only the integer count of edits: q for each vertex instead of floating-point values. The total edit at a vertex is simply computed as $\delta_i = q \cdot \xi/2^{q_{\max}}$. This significantly reduces storage overhead while ensuring the exact reconstruction of edited values. Since such cases are

relatively rare (as shown in Figure 13 (d)), this approach further reduces the need for floating-point storage, improving the overall compression ratio.

5 EVALUATION

We evaluate our method using datasets from various fields, including climate, combustion, cosmology, and molecular dynamics. SZ3 and ZFP are selected as the base compressors to generate the decompressed data. All datasets are defined on simply connected domains with regular grid-based triangulation, which aligns with our current implementation. We evaluate different values of q_{\max} and select $q_{\max} = 6$ based on a trade-off between storage and computational overhead. We also analyze the computational cost of different preservation tiers and evaluate the performance of TTHRESH; all results are reported in Appendix.

We highlight the experimental results in three aspects: First, DMTz preserves the full MSC under all tested error bounds, while both SZ3 and ZFP cause topological distortions to MSC, and the magnitude of distortion increases with the error bound, as reflected by the increasing number of required edits. Second, for preservation T1 through 4, the computation and storage overhead generally grow with the level of preservation, while T5 (persistence diagram) exhibits a distinct pattern, which we discuss in detail later. Additionally, our quantized edit strategy reduces the storage overhead compared to MSz [29]. Finally, our GPU-accelerated implementation achieves up to 855 \times speedup for gradient pairing, while separatrix extraction remains a performance bottleneck.

5.1 Evaluation Metrics

We evaluate our method using several key metrics. The **Critical/Separatrices Recalls** quantify the proportion of critical cells and separatrices in the original dataset that are successfully retained in the decompressed data. **Critical/Separatrices Precisions** quantify the proportion of detected critical cells and separatrices in the decompressed data that also exist in the original data. The **L^2 -Wasserstein Distance (W_2)** [10] represents the topological difference between the persistence diagrams of the original and decompressed data, with lower values indicating better preservation of persistent features. The **Compression Ratio (CR)** measures the efficiency of compressing the original scalar field alone, computed as the size of the original data divided by the size of the decompressed data. The **Overall Compression Ratio (OCR)** quantifies the compression efficiency after incorporating compressed edits. It is computed as the original data size divided by the combined size of compressed edits and data. The **Edit Ratio** measures the proportion of modified data points necessary to fully preserve the MSC in the decompressed data and is calculated as the number of modified points divided by the total number of data points.

5.2 Comparison of Compressors across Error Bounds

We demonstrate the ability of our method to fully preserve the MSC with different compressors and error bounds across various datasets while maintaining acceptable storage overhead, as shown in Figure 11. The number of edits generally shows a proportional relationship with the error bounds. We also observed that the number of required edits increases with the complexity of the dataset; for instance, the average edit ratio is lower for the Adenine Thymine (AT) dataset compared to the other datasets.

Furthermore, the number of edits required by ZFP is generally lower than SZ3, and ZFP’s overall compression ratio is also lower than SZ3. This is because ZFP’s original compression ratio is typically lower than SZ3, which introduces fewer errors in the decompressed data, resulting in less distortion in the MSC and requiring fewer edits. We also observe a trade-off between the error bound and the preservation of MSC, where a higher error bound results in larger pointwise errors between the decompressed and original data, causing more severe distortion of the MSC.

5.3 Computation and Storage Overhead

We analyze the computation and storage overhead introduced by the edits across different tiers on the IVT dataset, as shown in Figure 12.

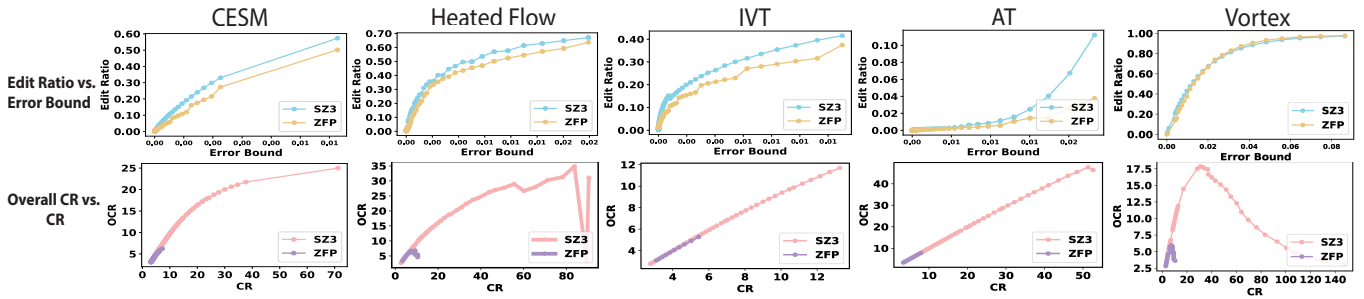


Fig. 11: Comparison of the capabilities of different lossy compressors to preserve MS complexes on different datasets across different error bounds.

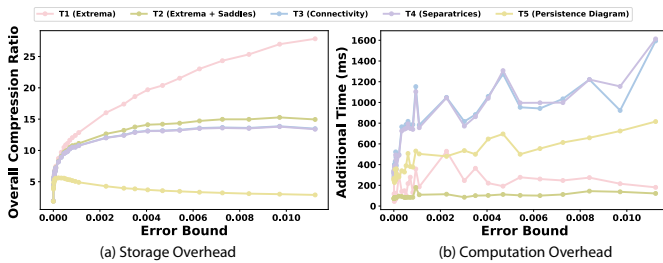


Fig. 12: Computation and Storage overhead of different tiers of preservation on the IVT dataset using SZ3 ranging from T1 (pink), T2 (brown), T3 (blue), T4 (purple), to T5 (yellow).

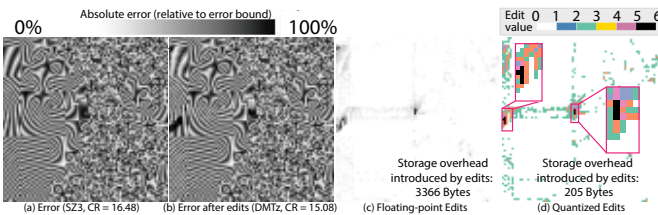


Fig. 13: Error maps and edit distributions on a cropped region of the Heated Flow dataset. (a) Error map of SZ3's decompressed data (relative error bound = 10^{-4}). (b) Error after applied edits (DMTz). (c) Edit values applied on SZ3's decompressed data. (d) Breakdown of quantized edits.

As preservation requirements increase, both computation and storage overheads generally increase (except for T5, discussed below). This trend is expected, as finer preservation imposes stricter constraints on allowable data changes, thus requiring more edits and longer correction procedures.

Among all tiers, T5 (persistence diagram preservation) exhibits a distinct trend: it incurs the highest storage overhead while maintaining relatively low computation cost, as shown in Figure 12(a) and (b). This trend is because preserving the persistence diagram requires strict enforcement of the relative ordering between critical points. In practice, we set the scalar value of each critical cell to be edited to its lower bound $f - \xi$, and these edits must be stored losslessly, resulting in substantial storage overhead. Once the critical cells are edited to their lower bounds, the discrete gradient field stabilizes more quickly, reducing the number of iterations required for addressing false separatrices or critical cells.

Furthermore, the quantized edits reduce the storage overhead by quantizing the majority of edits, compared to the floating-point edits used in MSz [29]. As illustrated in Figure 13(c) and (d), the quantization of edits reduces the storage overhead from 3366 bytes to 205 bytes in the Heated Flow dataset. A more detailed analysis of the compression of edits is provided in Appendix C.

5.4 Performance on GPUs

We assess the GPU performance of our algorithm on the Vortex dataset by analyzing five key components: (1) gradient pairing, (2) false critical cell extraction, (3) false separatrix extraction, (4) fix false critical cells, and (5) fix false separatrices. Experiments were conducted on a single

node with four NVIDIA A100 GPUs on the Perlmutter supercomputer at National Energy Research Scientific Computing (NERSC). All components were implemented in C++ and CUDA, executed 1,000 times, and averaged after resetting the data state to eliminate initialization variance.

Table 1 demonstrates the performance of our method on the Vortex dataset, including compute throughput (the ratio of executed floating-point operations to the hardware's peak performance) and memory throughput (the ratio of achieved memory bandwidth to the hardware's peak bandwidth). Gradient pairing achieved up to 855 \times speedup, owing to its highly local computations that parallelize well on GPUs. In contrast, extracting false separatrices showed relatively low throughput and speedups due to their reliance on graph traversal, but we still retain it on the GPU rather than offloading it to the CPU, driven by the significant overhead associated with data transfer. For example, in the task of extracting false saddle-saddle connectors, the GPU execution takes only 1.76 ms in this case, while transferring intermediate gradient pairing results to the CPU requires 48.92 ms—over 27 \times slower than computing directly on the GPU. By keeping all stages of the computation on the GPU, we eliminate transfer bottlenecks and ensure overall efficiency. The fix tasks also exhibit lower speedups, as they operate on a small subset of cells, leaving limited workload for parallelism. Another observation is that the compute and memory throughput vary across subtasks due to differences in algorithmic complexity and workload size. A formal analysis of compute vs. memory-bound behavior remains challenging and is deferred to future work.

Timings of different components also vary also over different iterations patterns, as shown in Figure 10. The first iteration incurs a higher cost from gradient pairing and false critical cell extraction due to numerous initial false critical cells, which trigger multiple C-loops. As iterations proceed, these costs drop and stabilize. This is because, in later iterations, the number of false critical cells in the data is significantly reduced or even eliminated, requiring only one or very few passes of gradient pairing and false critical cell extraction, and thus rarely entering C-loops. Meanwhile, separatrix-related tasks increasingly dominate, rising from 40% of runtime in early iterations to 60–70% later. Despite optimizations, this component remains the bottleneck, highlighting the need for future acceleration efforts.

6 DISCUSSION AND LIMITATION

We discuss the differences between DMTz and two related approaches, MSz and topological smoothing, and outline the limitations of DMTz.

6.1 Comparison of DMTz (ours) and MSz [29]

Our method is fundamentally different from MSz in terms of three aspects: theoretical assumptions, algorithmic complexity, and preservation capabilities, as discussed in the following.

Theoretical Assumptions. MSz assumes a piecewise linear scalar field defined on vertices and identifies critical points through local vertex comparisons. DMTz, by contrast, is based on discrete Morse functions, which require comparisons across cells of different dimensions, such as vertices, edges, and triangles.

Algorithmic Complexity. MSz computes segmentations by locally comparing the vertex values, making critical point detection relatively simple. DMTz requires gradient pairings across cells of different

Table 1: Average timings, GPU acceleration, and compute/memory throughput of various tasks in our algorithm on the Vortex dataset.

Task	Sub-task	Serial (ms)	CUDA (ms)	GPU Accel. cf. Serial	Compute Throughput (%)	Memory Throughput (%)
Gradient Pairing	Vertices	393.5	0.46	855×	87.62	24.87
	Edges	1866	2.76	676×	8.82	55.79
	Triangles	995.2	1.90	523×	19.95	60.05
Extract False Critical Cells	Minimum	10.05	0.04	251×	18.21	43.26
	1-Saddles	71.62	0.13	550×	22.97	53.54
	2-Saddles	129.4	0.20	647×	23.51	53.28
	Maximum	50.04	0.10	500×	22.99	55.03
Extract False Separatrices	Descending	48.92	0.18	271×	14.20	31.38
	Ascending	168.9	0.65	259×	13.72	17.25
	Saddle-Saddle	387.1	1.76	219×	17.55	32.50
Fix False Critical Cells	Minimum	0.19	0.01	19×	0.47	1.12
	1-Saddles	14.86	0.05	297×	14.60	6.13
	2-Saddles	75.62	0.42	180×	29.28	11.91
	Maximum	6.47	0.05	129×	4.78	9.18
Fix False Separatrices	Descending	1.17	0.007	167×	0.78	2.48
	Ascending	6.72	0.01	672×	9.39	15.55
	Saddle-Saddle	5.54	0.008	692×	1.92	21.89

dimensions, introducing more complex dependencies. For example, in a 2D case, a troublemaker in the ascending separatrix in MSz typically arises from the reversed scalar value ordering between two vertices, which can be corrected by editing a vertex. However, in DMTz, a troublemaker in the ascending separatrix can be a cell that either (1) incorrectly pairs with a vertex or (2) incorrectly pairs with a triangle. Each of these cases further splits into two subcases: (a) the cell was originally paired with a vertex, or (b) it was originally paired with a triangle. As a result, even in this relatively simple scenario, DMTz must resolve four distinct cases, making the correction process significantly more intricate. The complexity further increases in 3D, where 1-saddles and 2-saddles must also be handled, leading to additional error cases that do not exist in MSz.

Preservation Capabilities. MSz does not preserve saddle points or saddle-related structures, leading to topological inconsistencies such as false saddles, incorrect saddle-saddle or saddle-extrema connections. DMTz fully preserves all critical cells (including saddles) and ensures the correctness of separatrices, including 1-separatrices, 2-separatrices, and saddle connectors, which are not addressed by MSz.

6.2 Comparison of DMTz with Topological Smoothing

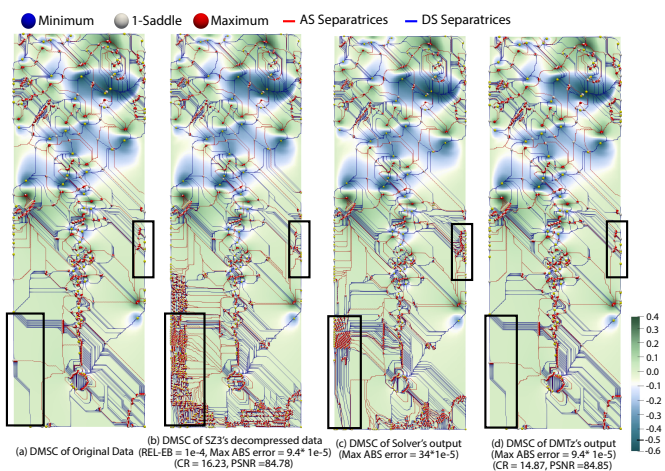


Fig. 14: Visualization of the DMSC structures of the heated flow dataset: (a) Original data, (b) SZ3's decompressed data, (c) Solver's output, and (d) DMTz's output. Black boxes highlight regions of structural differences.

Although one potential alternative for preserving topological structures in lossy compression is to store the original data's MSC and apply

Table 2: Comparison of topological smoothing and our method. The inputs are compressed under a relative error bound of 10^{-4}

	Original	Kissi et al. [25]	DMTz (Ours)
Min / Saddle / Max	98 / 703 / 606	158 / 1095 / 938	98 / 703 / 606
False critical cells	-	86 / 616 / 516	0 / 0 / 0
ABS Error Bound	9.4×10^{-5}	9.4×10^{-5}	9.4×10^{-5}
Max ABS Error	-	3.4×10^{-4}	9.4×10^{-5}
Separatrices Recall	1.00	0.38	1.00
Separatrices Precision	1.00	0.20	1.00
Critical Recall	1.00	0.84	1.00
Critical Precision	1.00	0.54	1.00
Runtime (s)	-	0.266	0.110
Storage Overhead (bytes)	-	157,122	3,541
		(MSC, CR = 2.84)	(Edits, CR = 14.87)

topological smoothing to the decompressed data that approximates the original MSC, this approach cannot fully preserve the complete MSC, as confirmed by our experimental results. In our experiment, we select the solver-based method proposed by Kissi et al. [25] (referred to as solver in the following), which is a fast, state-of-the-art implementation of topological smoothing. To evaluate its effectiveness, we compare the output of DMTz (ours) with that of the solver, using SZ3 as the base compressor with a relative error bound of 10^{-4} on the heated flow dataset. We used the original data's persistence diagram as the target for the solver to produce a smoothed version of the decompressed data. This comparison evaluates four key aspects: storage overhead, quantitative accuracy, topological alignment, and computational efficiency (see Table 2). **Storage Overhead.** Storing the entire MSC (critical points and separatrices) leads to a storage overhead of 157,122 bytes and an overall CR of 2.84. DMTz only stores 3,541 bytes of edits, achieving a CR of 14.87. **Quantitative Accuracy.** While the solver aligns the scalar field with the target persistence diagram, it lacks an error-bounded guarantee, resulting in a max absolute error of 3.4×10^{-4} , nearly 4x larger than SZ3's original absolute bound (9.4×10^{-5}). DMTz maintains the original error bound while preserving the MSC. **Topological Alignment.** The solver introduces numerous false critical points (86 minima, 616 saddles, 516 maxima), and its separatrices are distorted (Figure 14(c)), recovering only 61% of the original separatrices, whereas DMTz preserves 100%. **Computational Efficiency.** DMTz completes in 0.110s with full guarantees, outperforming the solver's 0.266s runtime by 2.4x.

6.3 Limitation

One limitation of our method is that it is tailored to the approach by Shivashankar et al. [46] for extracting MSC, so it inherits some drawbacks. For instance, their method can introduce many low-persistence critical points in noisy data, necessitating additional edits in our approach and leading to increased storage overhead. Additionally, the performance of false separatrix extraction remains a bottleneck, as it dominates the overall computation time in each iteration. Further optimization of this component is a direction for future work.

Another limitation is that our method does not consider preserving a simplified MSC. Conceptually, simplifying the target topological structure (e.g., by canceling low-persistence features) could reduce the number of critical points that need to be preserved and thus significantly reduce the storage overhead. Moreover, scientific analysis often requires simplification to focus on salient structures while filtering out noise, making it a valuable direction for future extension.

7 CONCLUSIONS AND FUTURE WORK

We introduced DMTz, an iterative workflow for preserving key topological features of the Morse-Smale complex (MSC) in error-bounded lossy compression. We also designed a multitier preservation paradigm to support different applications' preservation needs. By enabling the multitiered preservation of extrema, saddles, separatrices, and persistence diagrams, our method provides flexible options for balancing compression efficiency and feature preservation.

We plan to improve our method in various aspects. First, we will focus on preserving simplified MSC under a specific persistence threshold. Second, we plan to optimize the extraction of false separatrices to improve overall performance. Third, we intend to better handle noisy data by integrating our workflow with the DMSC extraction method of Robins et al. [45], reducing the impact of low-persistence critical points on computational and storage overhead.

REFERENCES

- [1] R. Ballester-Ripoll, P. Lindstrom, and R. Pajarola. TTHRESH: Tensor compression for multidimensional visual data. *IEEE Transactions on Visualization and Computer Graphics*, 26(9):2891–2903, 2020. doi: 10.1109/TVCG.2019.2904063 2
- [2] T. Banchoff. Critical points and curvature for embedded polyhedra. *Journal of Differential Geometry*, 1(3-4):245–256, 1967. doi: 10.4310/jdg/1214428092 3
- [3] H. Bhatia, A. G. Gyulassy, V. Lordi, J. E. Pask, V. Pascucci, and P.-T. Bremer. TMS: Comprehensive topological exploration for molecular and condensed-matter systems. *Journal of Computational Chemistry*, 39(16):936–952, 2018. doi: 10.1002/jcc.25181 1
- [4] P.-T. Bremer, G. Weber, V. Pascucci, M. Day, and J. Bell. Analyzing and tracking burning structures in lean premixed hydrogen flames. *IEEE Transactions on Visualization and Computer Graphics*, 16(2):248–260, 2010. doi: 10.1109/TVCG.2009.69 2
- [5] P.-T. Bremer, G. Weber, J. Tierny, V. Pascucci, M. Day, and J. Bell. Interactive exploration and analysis of large-scale simulations using topology-based data segmentation. *IEEE Transactions on Visualization and Computer Graphics*, 17(9):1307–1324, 2011. doi: 10.1109/TVCG.2010.253 2
- [6] H. Carr, J. Snoeyink, and U. Axen. Computing contour trees in all dimensions. *Computational Geometry*, 24(2):75–94, 2003. Special Issue on the Fourth CGC Workshop on Computational Geometry. doi: 10.1016/S0925-7721(02)00093-7 1
- [7] L. De Floriani, U. Fugacci, F. Iuricich, and P. Magillo. Morse complexes for shape segmentation and homological analysis: discrete models and algorithms. *Computer Graphics Forum*, 34(2):761–785, 2015. doi: 10.1111/cgf.12596 3, 4
- [8] S. Di, J. Liu, K. Zhao, X. Liang, R. Underwood, Z. Zhang, M. Shah, Y. Huang, J. Huang, X. Yu, C. Ren, H. Guo, G. Wilkins, D. Tao, J. Tian, S. Jin, Z. Jian, D. Wang, M. H. Rahman, B. Zhang, J. C. Calhoun, G. Li, K. Yoshii, K. A. Alharthi, and F. Cappelto. A survey on error-bounded lossy compression for scientific datasets, 2024. doi: 10.48550/arXiv.2404.02840 2
- [9] H. Doraiswamy, V. Natarajan, and R. S. Nanjundiah. An exploration framework to identify and track movement of cloud systems. *IEEE Transactions on Visualization and Computer Graphics*, 19(12):2896–2905, 2013. doi: 10.1109/TVCG.2013.131 1, 2
- [10] H. Edelsbrunner and J. Harer. *Computational Topology: An Introduction*. American Mathematical Society, 2009. doi: 10.1007/978-3-540-33259-6_7 7
- [11] H. Edelsbrunner, J. Harer, V. Natarajan, and V. Pascucci. Morse-Smale Complexes for piecewise linear 3-manifolds. In *Proceedings of the Nineteenth Annual Symposium on Computational Geometry*, SCG '03, 10 pages, pp. 361–370, 2003. doi: 10.1145/777792.777846 1
- [12] H. Edelsbrunner, J. Harer, and A. Zomorodian. Hierarchical Morse complexes for piecewise linear 2-manifolds. In *Proceedings of the Seventeenth Annual Symposium on Computational Geometry*, 10 pages, pp. 70–79, 2001. doi: 10.1145/378583.378626 1, 3
- [13] H. Edelsbrunner, D. Letscher, and A. Zomorodian. Topological persistence and simplification. In *Proceedings of 41st Annual Symposium on Foundations of Computer Science*, pp. 454–463, 2000. doi: 10.1109/SFCS.2000.892133 4
- [14] R. Forman. Morse theory for cell complexes. *Advances in Mathematics*, 134(1):90–145, 1998. doi: 10.1006/aima.1997.1650 3
- [15] R. Forman. A user’s guide to discrete Morse theory. *Sém. Lothar. Combin.*, 48, 12 2001. 3
- [16] Q. Gong, J. Chen, B. Whitney, X. Liang, V. Reshniak, T. Banerjee, J. Lee, A. Rangarajan, L. Wan, N. Vidal, Q. Liu, A. Gainaru, N. Podhorszki, R. Archibald, S. Ranka, and S. Klasky. MGARD: A multigrid framework for high-performance, error-controlled data compression and refactoring. *SoftwareX*, 24:101590, 2023. doi: 10.1016/j.softx.2023.101590 2
- [17] N. Gorski, X. Liang, H. Guo, L. Yan, and B. Wang. A general framework for augmenting lossy compressors with topological guarantees. *IEEE Transactions on Visualization and Computer Graphics*, 2025. in preprint. 1, 3
- [18] P. Gu, D. Z. Chen, and C. Wang. Nervi: Compressive neural representation of visualization images for communicating volume visualization results. *Computers & Graphics*, 116:216–227, 2023. doi: 10.1016/j.cag.2023.08.024 2
- [19] A. Gyulassy, M. Duchaineau, V. Natarajan, V. Pascucci, E. Bringa, A. Higinbotham, and B. Hamann. Topologically clean distance fields. *IEEE Transactions on Visualization and Computer Graphics*, 13(6):1432–1439, 2007. doi: 10.1109/TVCG.2007.70603 1
- [20] A. Gyulassy, V. Natarajan, V. Pascucci, P.-T. Bremer, and B. Hamann. A topological approach to simplification of three-dimensional scalar functions. *IEEE Transactions on Visualization and Computer Graphics*, 12(4):474–484, 2006. doi: 10.1109/TVCG.2006.57 3
- [21] D. Günther, R. A. Boto, J. Contreras-Garcia, J.-P. Piquemal, and J. Tierny. Characterizing molecular interactions in chemical systems. *IEEE Transactions on Visualization and Computer Graphics*, 20(12):2476–2485, 2014. doi: 10.1109/TVCG.2014.2346403 1
- [22] D. Günther, A. Jacobson, J. Reininghaus, H.-P. Seidel, O. Sorkine-Hornung, and T. Weinkauff. Fast and memory-efficiently topological denoising of 2D and 3D scalar fields. *IEEE Transactions on Visualization and Computer Graphics*, 20(12):2585–2594, 2014. doi: 10.1109/TVCG.2014.2346432 3
- [23] Y. Huang, S. Di, G. Li, and F. Cappelto. cuszp2: A GPU lossy compressor with extreme throughput and optimized compression ratio. In *Proceedings of the International Conference for High Performance Computing, Networking, Storage and Analysis*, pp. 1–18, 2024. 2
- [24] Y. Huang, S. Di, X. Yu, G. Li, and F. Cappelto. cuSZp: An ultra-fast GPU error-bounded lossy compression framework with optimized end-to-end performance. In *Proceedings of the International Conference for High Performance Computing, Networking, Storage and Analysis*, pp. 1–13, 2023. 2
- [25] M. Kissi, M. Pont, J. A. Levine, and J. Tierny. A practical solver for scalar data topological simplification. *IEEE Transactions on Visualization and Computer Graphics*, 31(1):97–107, 2025. doi: 10.1109/TVCG.2024.3456345 3, 9
- [26] S. Lakshminarasimhan, N. Shah, S. Ethier, S. Klasky, R. Latham, R. Ross, and N. F. Samatova. Compressing the incompressible with ISABELA: In-situ reduction of spatio-temporal data. In *Proceedings of the 17th International Conference on Parallel Processing - Volume Part I*, EuroPar’11, 14 pages, pp. 366–379, 2011. 2
- [27] F. Lan, B. Gamelin, L. Yan, J. Wang, B. Wang, and H. Guo. Topological characterization and uncertainty visualization of atmospheric rivers. *Computer Graphics Forum*, 43(3):e15084, 2024. doi: 10.1111/cgf.15084 2
- [28] S. Li, P. Lindstrom, and J. Clyne. Lossy scientific data compression with SPERR. In *Proceedings of 2023 IEEE International Parallel and Distributed Processing Symposium*, pp. 1007–1017, 2023. doi: 10.1109/IPDPS54959.2023.00104 2
- [29] Y. Li, X. Liang, B. Wang, Y. Qiu, L. Yan, and H. Guo. MSz: An efficient parallel algorithm for correcting Morse-Smale segmentations in error-bounded lossy compressors, 2024. 1, 2, 3, 4, 7, 8
- [30] X. Liang, S. Di, F. Cappelto, M. Raj, C. Liu, K. Ono, Z. Chen, T. Peterka, and H. Guo. Toward feature-preserving vector field compression. *IEEE Transactions on Visualization and Computer Graphics*, 29(12):5434–5450, 2023. doi: 10.1109/TVCG.2022.3214821 3
- [31] X. Liang, S. Di, D. Tao, S. Li, S. Li, H. Guo, Z. Chen, and F. Cappelto. Error-controlled lossy compression optimized for high compression ratios of scientific datasets. In *Proceedings of 2018 IEEE International Conference on Big Data*, pp. 438–447, 2018. doi: 10.1109/BigData.2018.8622520 1, 2, 3
- [32] X. Liang, H. Guo, S. Di, F. Cappelto, M. Raj, C. Liu, K. Ono, Z. Chen, and T. Peterka. Toward feature-preserving 2D and 3D vector field compression. In *Proceedings of 2020 IEEE Pacific Visualization Symposium*, pp. 81–90, 2020. doi: 10.1109/PacificVis48177.2020.6431 1
- [33] X. Liang, H. Guo, S. Di, F. Cappelto, M. Raj, C. Liu, K. Ono, Z. Chen, and T. Peterka. Toward feature-preserving 2D and 3D vector field compression. In *Proceedings of 2020 IEEE Pacific Visualization Symposium*, pp. 81–90, 2020. doi: 10.1109/PacificVis48177.2020.6431 3
- [34] X. Liang, K. Zhao, S. Di, S. Li, R. Underwood, A. M. Gok, J. Tian, J. Deng, J. C. Calhoun, D. Tao, Z. Chen, and F. Cappelto. SZ3: A

- modular framework for composing prediction-based error-bounded lossy compressors. *IEEE Transactions on Big Data*, 9(2):485–498, 2023. doi: 10.1109/TBDDATA.2022.3201176 1, 2
- [35] P. Lindstrom. Fixed-rate compressed floating-point arrays. *IEEE Transactions on Visualization and Computer Graphics*, 20(12):2674–2683, 2014. doi: 10.1109/TVCG.2014.2346458 1, 2
- [36] P. Lindstrom and M. Isenburg. Fast and efficient compression of floating-point data. *IEEE Transactions on Visualization and Computer Graphics*, 12(5):1245–1250, 2006. doi: 10.1109/TVCG.2006.143 1, 2
- [37] J. Liu, S. Di, S. Jin, K. Zhao, X. Liang, Z. Chen, and F. Cappello. SRN-SZ: Deep leaning-based scientific error-bounded lossy compression with super-resolution neural networks, 2023. 2
- [38] J. Liu, S. Di, K. Zhao, S. Jin, D. Tao, X. Liang, Z. Chen, and F. Cappello. Exploring autoencoder-based error-bounded compression for scientific data. In *Proceedings of 2021 IEEE International Conference on Cluster Computing (CLUSTER)*, pp. 294–306, 2021. doi: 10.1109/Cluster48925.2021.00034 2
- [39] J. Liu, S. Di, K. Zhao, X. Liang, Z. Chen, and F. Cappello. Dynamic quality metric oriented error bounded lossy compression for scientific datasets. In *Proceedings of International Conference for High Performance Computing, Networking, Storage and Analysis*, pp. 62:1–62:15, 2022. doi: 10.1109/SC41404.2022.00067 2
- [40] T. Liu, J. Wang, Q. Liu, S. Alibhai, T. Lu, and X. He. High-ratio lossy compression: Exploring the autoencoder to compress scientific data. *IEEE Transactions on Big Data*, 9(1):22–36, 2023. doi: 10.1109/TBDDATA.2021.3066151 2
- [41] Y. Lu, K. Jiang, J. A. Levine, and M. Berger. Compressive neural representations of volumetric scalar fields. *Computer Graphics Forum*, 40(3):135–146, 2021. doi: 10.1111/cgf.14295 2
- [42] R. G. C. Maack, J. Lukasczyk, J. Tierny, H. Hagen, R. Maciejewski, and C. Garth. Parallel computation of piecewise linear Morse-Smale segmentations. *IEEE Transactions on Visualization and Computer Graphics*, 30(4):1942–1955, 2024. doi: 10.1109/TVCG.2023.3261981 1
- [43] T. B. Masood, J. Budin, M. Falk, G. Favelier, C. Garth, C. Gueunet, P. Guilou, L. Hofmann, P. Hristov, A. Kamakshidasan, et al. An overview of the topology toolkit. *Topological Methods in Data Analysis and Visualization VI: Theory, Applications, and Software*, pp. 327–342, 2021. 2, 4
- [44] S. Petruzza, A. Gyulassy, S. Leventhal, J. J. Baglino, M. Czabaj, A. D. Spear, and V. Pascucci. High-throughput feature extraction for measuring attributes of deforming open-cell foams. *IEEE Transactions on Visualization and Computer Graphics*, 26(1):140–150, 2020. doi: 10.1109/TVCG.2019.2934620 1
- [45] V. Robins, P. J. Wood, and A. P. Sheppard. Theory and algorithms for constructing discrete Morse complexes from grayscale digital images. *IEEE Transactions on Pattern Analysis and Machine Intelligence*, 33(8):1646–1658, 2011. doi: 10.1109/TPAMI.2011.95 3, 10
- [46] N. Shivashankar and V. Natarajan. Parallel computation of 3D Morse-Smale complexes. *Computer Graphics Forum*, 31(3pt1):965–974, 2012. doi: 10.1111/j.1467-8659.2012.03089.x 3, 4, 9
- [47] N. Shivashankar, P. Pranav, V. Natarajan, R. v. d. Weygaert, E. P. Bos, and S. Rieder. Felix: A topology based framework for visual exploration of cosmic filaments. *IEEE Transactions on Visualization and Computer Graphics*, 22(6):1745–1759, 2016. doi: 10.1109/TVCG.2015.2452919 1
- [48] P. Skraba, B. Wang, G. Chen, and P. Rosen. Robustness-based simplification of 2D steady and unsteady vector fields. *IEEE Transactions on Visualization and Computer Graphics*, 21(8):930–944, 2015. doi: 10.1109/TVCG.2015.2440250 3
- [49] M. Soler, M. Plainchault, B. Conche, and J. Tierny. Topologically controlled lossy compression. In *Proceedings of 2018 IEEE Pacific Visualization Symposium*, pp. 46–55, 2018. doi: 10.1109/PacificVis.2018.00015 3
- [50] D. Tao, S. Di, Z. Chen, and F. Cappello. Significantly improving lossy compression for scientific data sets based on multidimensional prediction and error-controlled quantization. In *Proceedings of 2017 IEEE International Parallel and Distributed Processing Symposium*, pp. 1129–1139, 2017. doi: 10.1109/IPDPS.2017.115 1, 2
- [51] H. Theisel, C. Ross, and H.-P. Seidel. Combining topological simplification and topology preserving compression for 2D vector fields. In *Proceedings of Pacific Conference on Computer Graphics and Applications, 2003.*, pp. 419–423, 2003. doi: 10.1109/PCCGA.2003.1238287 3
- [52] J. Tierny and V. Pascucci. Generalized topological simplification of scalar fields on surfaces. *IEEE Transactions on Visualization and Computer Graphics*, 18(12):2005–2013, 2012. doi: 10.1109/TVCG.2012.228 3
- [53] X. Tricoche, G. Scheuermann, and H. Hagen. Continuous topology simplification of planar vector fields. In *Proceedings of Visualization, 2001. VIS'01.*, pp. 159–166. IEEE, 2001. 3
- [54] T. Weinkauff, Y. Gingold, and O. Sorkine. Topology-based smoothing of 2D scalar fields with c1-continuity. *Computer Graphics Forum*, 29(3):1221–1230, 2010. doi: 10.1111/j.1467-8659.2009.01702.x 3
- [55] T. Weinkauff, H. Theisel, K. Shi, H.-C. Hege, and H.-P. Seidel. Extracting higher order critical points and topological simplification of 3D vector fields. In *VIS 05. IEEE Visualization, 2005.*, pp. 559–566, 2005. doi: 10.1109/VISUAL.2005.1532842 3
- [56] M. Xia, S. Di, F. Cappello, P. Jiao, K. Zhao, J. Liu, X. Wu, X. Liang, and H. Guo. Preserving topological feature with sign-of-determinant predicates in lossy compression: A case study of vector field critical points. In *2024 IEEE 40th International Conference on Data Engineering (ICDE)*, pp. 4979–4992, 2024. doi: 10.1109/ICDE60146.2024.00378 1, 3
- [57] M. Xia, B. Wang, Y. Li, P. Jiao, X. Liang, and H. Guo. Tpspsz: An efficient parallel error-bounded lossy compressor for topological skeleton preservation. In *2025 IEEE 41st International Conference on Data Engineering (ICDE)*, 2025(In Press). 3
- [58] Z. Xu. Medical image fusion using multi-level local extrema. *Information Fusion*, 19:38–48, 2014. Special Issue on Information Fusion in Medical Image Computing and Systems. doi: 10.1016/j.inffus.2013.01.001 1, 2
- [59] L. Yan, X. Liang, H. Guo, and B. Wang. TopoSZ: Preserving topology in error-bounded lossy compression. *IEEE Transactions on Visualization and Computer Graphics*, 30(1):1302–1312, 2024. doi: 10.1109/TVCG.2023.3326920 1, 3
- [60] K. Zhao, S. Di, M. Dmitriev, T.-L. D. Tonellot, Z. Chen, and F. Cappello. Optimizing error-bounded lossy compression for scientific data by dynamic spline interpolation. In *Proceedings of 2021 IEEE 37th International Conference on Data Engineering*, pp. 1643–1654, 2021. doi: 10.1109/ICDE51399.2021.00145 1, 2
- [61] K. Zhao, S. Di, X. Liang, S. Li, D. Tao, Z. Chen, and F. Cappello. Significantly improving lossy compression for HPC datasets with second-order prediction and parameter optimization. In *Proceedings of the 29th International Symposium on High-Performance Parallel and Distributed Computing*, 12 pages, pp. 89–100, 2020. doi: 10.1145/3369583.3392688 1